Chinese Chemical Letters 35 (2024) 108681

Contents lists available at ScienceDirect

Chinese Chemical Letters

journal homepage: www.elsevier.com/locate/cclet

Scalable production of mesoporous titanium nanoparticles through sequential flash nanocomplexation

Feng Cui[a,e,1], Fangman Chen[a,e,1], Xiaochun Xie[b,e], Chenyang Guo[a,e], Kai Xiao[b,e], Ziping Wu[c,e], Yinglu Chen[c,e], Junna Lu[a,e], Feixia Ruan[b,e], Chuanxu Cheng[a,e], Chao Yang[a,d,*], Dan Shao[a,b,e,*]

[a] *School of Biomedical Sciences and Engineering, South China University of Technology, Guangzhou International Campus, Guangzhou 511442, China*
[b] *Institutes for Life Sciences, School of Medicine, South China University of Technology, Guangzhou 510006, China*
[c] *School of Biology and Biological Engineering, South China University of Technology, Guangzhou 510006, China*
[d] *Department of Orthopedics, Academy of Orthopedics-Guangdong Province, Orthopedic Hospital of Guangdong Province, Guangdong Provincial Key Laboratory of Bone and Joint Degenerative Diseases, The Third Affiliated Hospital of Southern Medical University, Guangzhou 510665, China*
[e] *National Engineering Research Center for Tissue Restoration and Reconstruction, South China University of Technology, Guangzhou 510006, China*

ARTICLE INFO

Article history:
Received 19 April 2023
Revised 9 June 2023
Accepted 11 June 2023
Available online 15 June 2023

Keywords:
Mesoporous titanium nanoparticles
Flash nanocomplexation
Photocatalytic
Antibacterial
Sequential

ABSTRACT

Mesoporous titanium nanoparticles (MTNs) have emerged as an important porous semiconductor owning to their large surface area and unique electronic/optical properties. However, the fundamental research for rational manufacturing MTNs in a highly scalable manner remains a challenge. In this study, we report a two-step flash nanocomplexation (FNC) approach to large-scalable generate MTNs through the sequential combination of two multi-inlet vortex mixers. By optimizing the concentrated titanium precursor, polyethylene glycol (PEG)-functionalized silane amount and pH, we have been able to produce MTNs with small particle size (31.5 nm), larger surface area (416.9 m^2/g) and pore volume (0.59 cm^3/g). Different from the traditional MTNs bulk, FNC-produced MTNs exhibited well-controlled manner and exceptional photocatalytic and antibacterial properties. Importantly, the optimized MTNs outperformed commercial P25 not only in protecting ultraviolet A (UVA)-exposed skin, but also in treating *P. aeruginosa*-infected wound. We believe that the high controllability and scalability of sequential flash nanocomplexation method offers great opportunities in enhancing the performance of mesoporous titanium nanoparticles.

Titanium dioxide (TiO_2) is a well-established material with a long history of use as a white pigment. Its affordable cost, chemical stability, environmental friendliness, and biocompatibility have attracted substantial attention in recent decades [1]. The discovery by Fujishima and Honda in 1972 of the photocatalytic splitting of water on TiO_2 electrodes for hydrogen production has unveiled the wide-ranging potential of titanium dioxide in the field of photocatalysis [2]. This discovery not only led to the identification of the broad potential of TiO_2 in photocatalysis but also inspired extensive investigation of its photocatalytic properties [3–6]. TiO_2 is employed in diverse areas, including degrading organic waste in water and air [7], acting as a sunscreen against ultraviolet (UV) damage [8,9], and killing bacterial through light irradiation [10]. In this context, nanoparticulate titanium dioxides especially commercial Degussa TiO_2 P25 contribute to the technological application including photocatalysis, batteries, sensors, and optoelectronic devices. Mesoporous titanium nanoparticles (MTNs) exhibit a higher specific surface area and larger pore volume compared to traditional TiO_2 nanoparticles. The abundance of active sites on surface and interface of MTNs facilitates the diffusion of reactants and products for adsorption and catalysis [11–15]. The well-known sol-gel method is a conventional approach for MTNs synthesis through targeting the process of hydrolysis and condensation [16]. However, MTNs from self-assembly to date irregulate structure and large size, mainly attributed to two sequential phase, the rapid hydrolysis of titanium precursor and subsequent uncontrolled condensation and termination [17]. In addition to this, scale-up of nanoformulations feature fabrication and reproducibility of manufacturing remain key challenges, in particular for the nanoparticles with small size and complex structure, which can be time consuming and require specialized equipment. From these considerations, the development of refined synthetic methods al-

---

[*] Corresponding authors.
E-mail addresses: charisyang910@gmail.com (C. Yang), shaodan@scut.edu.cn (D. Shao).

[1] These authors contributed equally to this work.

https://doi.org/10.1016/j.cclet.2023.108681

lowing MTNs to be tailored with the control of indiscriminate hydrolysis and condensation can facilitate their performance in commercial application.

Flash-based technology, the combination of rapid mixing technique with the self-assembly of molecules, generates nanoformulations in a continuous manner [18–21]. Flash nanocomplexation (FNC) is a kinetically controlled mixing process adapted from flash nanoprecipitation, which was driven by ionic, hydrophobic, hydrogen bonding, metal coordination, and specific ligand or host-guest interactions. To achieve uniform phase separation and nanoformation, a multi-inlet vortex mixer (MIVM) is employed to facilitate rapid and efficient turbulent mixing of two or more solutions, allowing scalable, repeatable, and robust fabrication of diverse nanoformations with well-controlled structure, composition, size, and surface properties for a more expansive range of potential applications [22,23]. Specifically, the utilization of the FNC has been demonstrated to accelerate the diffusion of molecules, thereby promoting rapid nucleation and self-assembly into the corresponding nanostructures [24–26]. Based on these findings, we hypothesize that FNC hold great promise on controlling the hydrolysis and condensation process during the production of MTNs. However, combining all the building materials into one MIVM could not regulate the sequence of hydrolysis and condensation at very short time, leading to the uncontrolled fabrication of MTNs. Thus, development of reliable FNC-based approaches for constructing controlled MTNs through ordered reaction sequence remains highly desirable.

To circumvent these problems, we designed a two-step flash nanocomplexation approach with sequential combination of two MIVMs for the rapid and scalable fabrication of MTNs. By initiating nucleation and growth in the first MIVM and subsequently sealing the formed nanoparticles with the second MIVM, the growth process can be effectively controlled to prevent further expansion. We systematically investigated how the size and structure of MTNs can be regulated by tuning the concentration of titanium precursor, polyethylene glycol (PEG)-functionalized silane and pH. Having optimized the best-performing MTNs and characterized their pore properties, we compared the photocatalytic and antibacterial properties between FNC-produced MTNs, MTNs bulk, and commercial P25 *in vitro*. Finally, we demonstrated the advantages of FNC-produced MTNs in the treatment of UV damage resistance of skin and *P. aeruginosa*-infected wound healing *in vivo*. Our study provides a promising sequential FNC approach for the scalable fabrication of sophisticated nanoformulations with ordered structures.

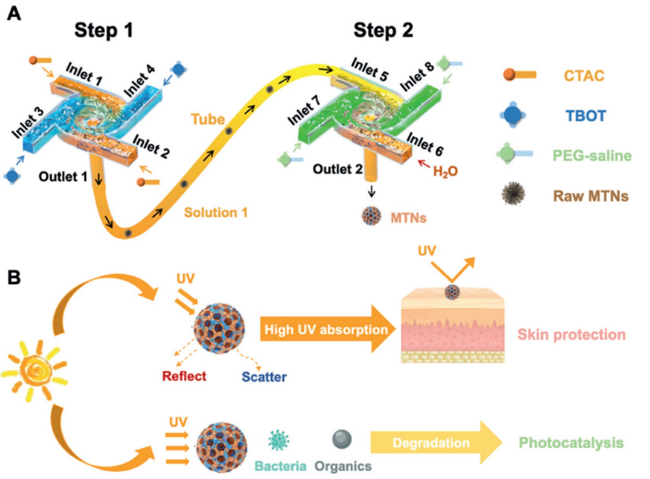

Scheme 1. Schematic illustration of the development of the two-step flash nanocomplexation (FNC) process to fabricate mesoporous titanium nanoparticles (MTNs) for biomedical applications. (A) Synthesis of the MTNs with sequential FNC method. (B) MTNs enabled ultraviolet absorption and photocatalytic properties to degrade organic waste and kill bacteria.

Although MTNs have been widely prepared by so-gel bulk methods [27], generating MTNs with smaller size and regular morphology remains a challenge. In this study, we developed a sequential system through ordered combination of two MIVMs to fabricate MTNs at a short time scale (Scheme 1A). In the first MIVM, titanium precursor and surfactant were co-injected to produce MTNs without surface modification. Then, such raw nanomaterials were immediately transferred into the second MIVM with the aid of PEG-functionalized silane to stop the growth of TiO_2. We systematically investigated into how the concentration of titanium precursors, PEG-silane and pH affect the size and morphology of MTNs (Figs. S1–S3 in Supporting information). We found that increasing the concentration of titanium precursors from 0.075 mmol/mL to 0.5 mmol/mL induced very different size and morphology, the middle concentration (0.3 mmol/mL) led to the most regular morphology with the smallest size. The concentration of PEG-silane at 0.15 mmol/mL made more uniform morphology of MTNs. After tuning the pH from 5 to 10, we demonstrated the optimized pH for the best nanoparticulate size and morphology was 8. Collectively, the regulation of the concentrated titanium precursors, PEG-silane and pH were crucial in achieving uniform particle size. Moreover, we investigated how velocity ratios between surfactant and titanium precursors in the first MIVM affect the size of products (Fig. S4 in Supporting information). We confirmed that the size of MTNs was decreased with the increasing the velocity ratios from 1:1 to 5:1, providing the optimal condition of surfactant/titanium precursors ratio at 5:1. Based on these findings, we prepared the outperforming MTNs with the optimal concentration of titanium precursors (0.3 mmol/mL) and PEG-silane (0.15 mmol/mL), pH 8, and surfactant/titanium precursors ratio (5:1). After calcination at 500 °C for 4 h, the FNC-based MTNs (referred to as "MTNs" for simplicity) were obtained. In parallel, we prepared control MTNs through single MIVM or bulk method (referred to as "BULK" for simplicity) (Fig. S5 in Supporting information). Scanning electron microscopy (SEM) and transmission electron microscope (TEM) revealed the outperforming MTNs to be uniformly spherical with a size of approximately 31.5 nm with a mesoporous structure (Figs. 1A and B). In contrast, both single MIVM- and BULK-based MTNs exhibited irregular size and morphology including uneven size distribution, morphology collapse and severe aggregation. X-ray diffraction (XRD) patterns indicated the presence of both anatase (JCPDS No. 21–1272) and rutile (JCPDS No. 21–1276) phases (Fig. 1C), which have better photocatalytic activity. The nitrogen adsorption-desorption isotherms of MTNs belongs to typical type IV adsorption curve, showed bimodal mesopore distributions with high surface area and pore volume, as calculated using the Brunauer-Emmett-Teller (BET) method. The BET surface area and pore volume of outperforming MTNs were 461.9 m^2/g and 0.59 cm^3/g (Fig. 1D), respectively, which were significantly higher than those of single MIVM-based MTNs (167.8 m^2/g and 0.27 cm^3/g), BULK (180.4 m^2/g and 0.34 cm^3/g), as well as commercial P25 (85.7 m^2/g and 0.23 cm^3/g). The pore size of MTNs, calculated using the Barrett-Joyner-Halenda (BJH) model, revealed the presence of pores with diameters centered at 6.5 nm (the inset in Fig. 1D), which was considerably larger than that of single MIVM-based MTNs (0.9 nm), BULK (1.2 nm), and P25 (1.5 nm) (Fig. S5). Taken together, these findings demonstrated the advantages of sequential FNC-based MTNs in the regular size, morphology and pore properties, indicating their outstanding performance on photocatalytic and antibacterial activities. Drawing on prior investigations and existing theories surrounding MTNs preparation, we presented a coherent conceptualization of the growth mechanism underlying the formation of MTNs. In the first MIVM, the formation of template micelle was initiated by the violent mixing of hydrophobic tetrabutyl titanate (TBOT) molecules in ethanol phase and *N*-

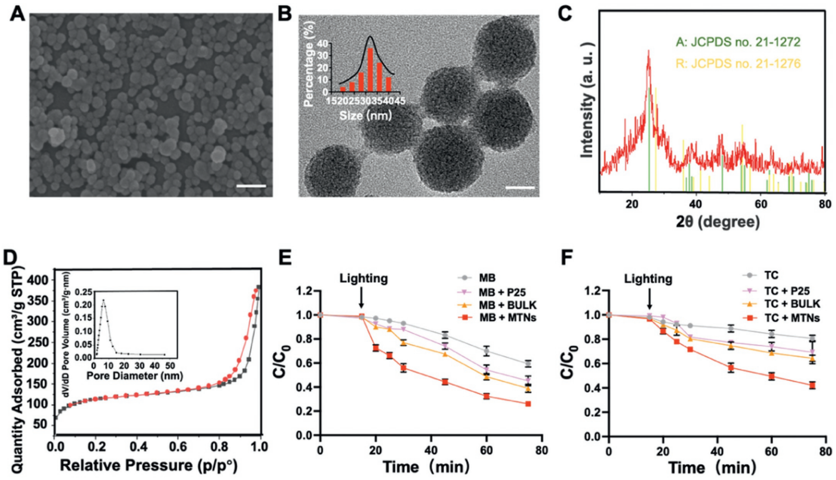

Fig. 1. Characterization of MTNs. (A) SEM image (scale bar, 100 nm) and (B) TEM image (scale bar, 20 nm) of the mesoporous titanium nanoparticles. (C) XRD patterns of the mesoporous titanium nanoparticles compared with the standard rutile (R) and anatase (A). (D) Nitrogen adsorption-desorption isotherms and pore-size distribution (inset) of the mesoporous titanium nanoparticles. Photocatalytic efficiency for the degradation of (E) methylene blue and (F) tetracycline. Results are shown as mean ± standard deviation (SD) ($n = 3$).

hexadecyltrimethylammonium chloride (CTAC) in aqueous phase within MIVM's minuscule mixing chamber, resulting in the formulation with TBOT/ethanol phase inside and water outside. Subsequently, the TBOT molecules inside the cores of templates diffused out and underwent hydrolysis at the outside water-rich interface. In view of the high hydrolysis and condensation rate of TBOT, the hydrolysis reaction must be terminated swiftly to produce MTNs with small and controllable particles in the second MIVM. Thus, we introduced the capping agent PEG-silane in the second step to prevent TBOT from further contact with water, ultimately bringing the entire reaction to an end to generate MTNs. For the single MIVM-based production, the hydrolysis, condensation, and termination of the titanium precursor occur at the same time when CTAC and TBOT were concurrently present within single MIVM device, leading to the irregular growth of MTNs due to the immediately disturbance of PEG-silane. For the BULK-based production, the titanium precursor might hydrolyze completely before the introduction of PEG-silane due to the rapid hydrolysis rate of titanium precursor, resulting in the overgrowth of MTNs. Different from these two methods, our sequential MIVM-based production separated the process of hydrolysis, condensation and terminalization in different MIVMs, offering strong and interference-free driving force for the sophisticated fabrication of MTNs with regulated size, morphology and pore structures.

The suitability of TiO_2 as a photocatalyst has been substantiated by its favorable band gap and position, elevated quantum efficiency and sustained stability. Consequently, this material has found extensive application in the elimination of contaminants during water and air purification [28,29]. To assess the catalytic performance of MTNs for organic matter decomposition, methylene blue (MB) and tetracycline (TC) were selected as model pollutants to measure the change in their respective colors. As shown in Fig. 1E, the degradation of MB was found to be significantly more efficient with MTNs than with other groups upon the exposure to light, with MTNs degrading approximately half of the MB within a 10 min timeframe. In contrast, both BULK and P25 required at least 30 min to achieve the same level of degradation. Similarly, it was observed that approximately 50% of the total TC was degraded within a 30-min timeframe when exposed to light with MTNs, while the BULK and P25 groups only achieved approximately 35% TC degradation in a 75-min timeframe (Fig. 1F). These findings demonstrated that MTNs exhibited superior catalytic activity compared to the P25 and BULK under light conditions. Furthermore, the catalytic efficiency of MTNs was notably enhanced under light irradiation, highlighting the significance of illumination in promoting MTNs' catalytic performance. This phenomenon might be attributed to the semiconductor property of TiO_2 with a band gap of approximately 3.0 eV, which enabled the excitation of electrons and holes when exposed to UV light (with wavelengths shorter than ~400 nm). The photogenerated electrons then react with O_2 to produce $^{\cdot}O_2^-$, while the photogenerated holes react with water to produce $^{\cdot}OH$ [30–33]. These reactive radicals worked together to decompose organic compounds. The prolonged exposure of the TiO_2 to UV light lead to the degradation of a greater quantity of organic material, indicating the excellent catalytic performance of MTNs might have great potential in bacterial killing under light irradiation.

In this study, we conducted a systematic investigation into the antibacterial properties of MTNs, BULK, and P25. In order to ascertain the effectiveness of the treatment, an evaluation was performed on the bacterial growth curves, and contact sterilization assays were carried out, respectively. As a proof of concept, Gram-negative *E. coli*, *P. aeruginosa* and Gram-positive *S. aureus* were chosen as model bacteria assays. As shown in Figs. 2A–C, we found that the OD_{600} values of the control group in all three bacterial strains significantly increased after 3 h. However, the OD_{600} values of MTNs group did not increase after 24 h of light irradiation. MTNs demonstrated a 100% bacterial killing efficiency in all three bacterial strains, while both BULK and P25 did not exhibit a significant antibacterial effect. In this study, the minimum inhibitory concentrations (MICs) of MTNs, BULK, and P25 were determined against three bacterial strains, *E. coli*, *S. aureus*, and *P. aeruginosa*. The MIC values for MTNs against *E. coli*, *S. aureus*, and *P. aeruginosa* were found to be 125, 62.5, and 62.5 µg/mL, respectively, as depicted in Fig. 2D. On the other hand, the MIC values for BULK against the same bacterial strains were found to be 250, 500, and 250 µg/mL, respectively. Similarly, for P25, the MIC values against the three bacterial strains were found to be 500, 500, and 250 µg/mL. These findings collectively confirmed that FNC-produced MTNs exhibited greater light-activable anti-bacterial effect than BULK and P25. Correspondingly, the antimicrobial properties of MTNs were evaluated through a systematic diffusion analysis conducted on agar plates. We found that only the MTNs group completely inhibited bacterial growth after 24 h of light irradiation in all three bacterial strains (Fig. 2E and Fig. S6 in Supporting information). However, the bacterial colonies were obvious in plates containing equal con-

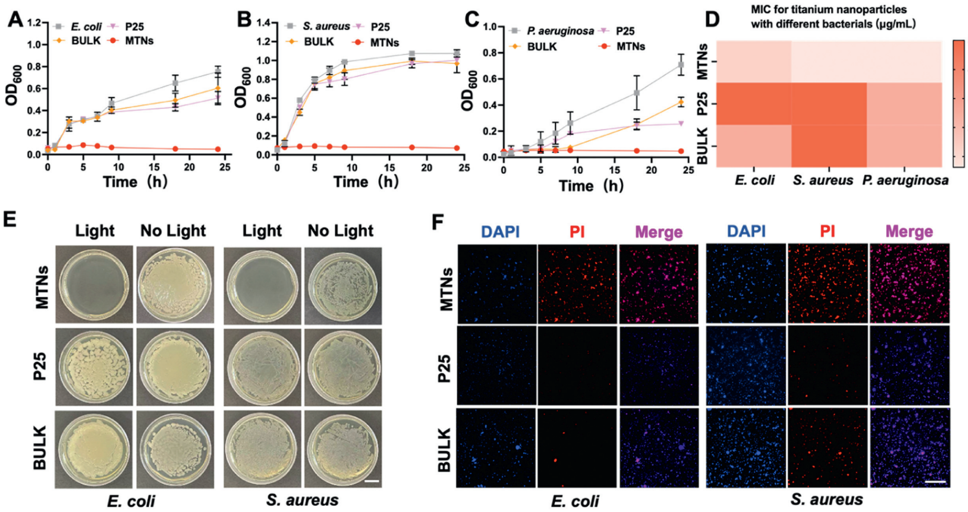

Fig. 2. *In vitro* antibacterial activity of the MTNs. (A–C) Growth curves of *E. coli*, *S. aureus*, and *P. aeruginosa* after incubating with MTNs, P25, and BULK for 24 h. (D) Heat map of the MIC for MTNs, P25, and BULK against bacteria for 24 h. (E) Surface antibacterial behaviors of MTNs, P25, and BULK (scale bar, 10 mm). (F) Living and dead bacteria staining of MTNs, P25, and BULK (scale bar, 100 µm). Results are shown as mean ± SD ($n = 3$). PI, propidium iodide; DAPI, 4′,6-diamidino-2-phenylindole.

centrations of BULK or P25. Consistently, the observation from living and dead bacteria staining indicated that only MTNs demonstrated almost 100% bacterial killing efficiency (Fig. 2F and Fig. S6). We attributed these superior surface antibacterial effects of MTNs to their small size and large mesoporous structure, which enabled more efficient photocatalytic performance and greater production of radicals that could destroy bacterial membranes. Taken together, these findings demonstrated that MTNs exhibited excellent antibacterial ability against multiple bacterial strains, making them an appealing candidate for the treatment of bacterial-infected wounds [34–36].

Having demonstrated the potent antibacterial properties of MTNs under light irradiation, we aimed to evaluate their sunlight-activable performance on promoting wound healing in a *P. aeruginosa*-infected wound model [37,38]. All animal experiments were conducted in agreement with the guidelines outlined in the Guide for the Care and Use of Laboratory Animals, and the procedures were approved by the Institutional Animal Care and Use Committee of South China University of Technology (Guangzhou, China). We created a round wound of 10 mm diameter on the back of mice and infected the wound with *P. aeruginosa* to develop a wound infection model. We treated the *P. aeruginosa*-challenged mice with phosphate buffered saline (PBS) (as a model), MTNs, BULK, and P25 under the exposure of sunlight for 14 days, while injured mice without infection served as a control group (Fig. 3A). The representative images of the wounds at every 3 or 4 days were presented in Fig. 3B. Mice treated with MTNs, BULK, and P25 outperformed *P. aeruginosa*-infected mice on the acceleration of wound healing. Notably, the infected wound treated with MTNs exhibited faster wound healing than BULK or P25-treated mice. On day 6, the MTNs group showed a significantly smaller wound area, while there was no significant change in other groups. By day 14, wounds treated with MTNs were almost completely healed, while those treated with other materials were still open. Corresponding wound area changes diagram (Fig. 3C) was consistent with the results of wound photos. Furthermore, the closure rate of the wound at various time points was computed and illustrated (Fig. 3D). Correspondingly, the wound area of the MTNs group (63.19%) was significantly smaller than which of the control (77.93%), model (90.53%), BULK (76.52%), and P25 groups (85.94%) after 6 days of treatment. Consistently, the application of MTNs resulted in nearly complete wound closure, as evidenced by a mean wound area of 4.64%, a statistically significant reduction compared to the model group (24.93%), BULK (15.35%), and P25 (16.63%) groups after 14 days of treatment. These findings together demonstrated that MTNs remarkably accelerated *P. aeruginosa*-challenged wound healing under the exposure of sunlight.

Bacterial infection and excessive inflammation seriously delay the chronic wounds healing [39–42]. The levels of tumor necrosis factor-α (TNF-α) and interleukin-6 (IL-6) were significantly lower in the MTNs group compared with other groups after treatment (Figs. 3E and F). Histological analysis of wound specimens was performed on day 14 to assess the healing and regeneration process (Fig. 3G). The tissue hematoxylin and eosin (H&E) staining images showed that the epidermal thickness of the MTNs group was the highest in experimental groups, indicating that MTNs had the best wound healing activity after light irradiation (Fig. 3H). Furthermore, Masson's trichrome staining showed the potential impact of MTNs on the promotion of collagen formation and deposition (Fig. 3I). Immunohistochemistry staining of CD31 was performed to evaluate the neovascularization and angiogenesis of wound sites. We observed that wounds treated with MTNs expressed more CD31 than other groups, indicating the formation of mature blood vessels and new capillaries (Fig. 3J). These results suggested that light-triggered MTNs promoted the healing of *P. aeruginosa*-infected wounds by facilitating collagen deposition and angiogenesis. Following a 14-day period of treatment, the biosafety profile of MTNs was evaluated by the H&E staining of collected major organs including heart, liver, spleen, lung, and kidney. The pathological sections demonstrated no observable damage in all treatment groups (Fig. S7A in Supporting information). Furthermore, serum biochemical biomarkers of alanine transaminase (ALT), aspartate transaminase (AST), blood urea nitrogen (BUN), and creatinine (CRE) were analyzed to assess the potential systemic toxicity associated with MTNs, BULK, and P25 treatment (Figs. S7B–E in Supporting information). There were no significant changes in serum biochemical biomarkers, together demonstrating that all titanium nanoparticles did not induce obvious systematic toxicity during the light-based treatment.

Encouraged by these findings, we supposed that MTNs might exhibit photoprotection to ultraviolet A (UVA)-exposed skin after being loaded with oxybenzone (OBZ), an approved UVA organic filter to avoid photoaging. We thus prepared three kinds of OBZ-loaded titanium nanoparticles. The loading content of OBZ

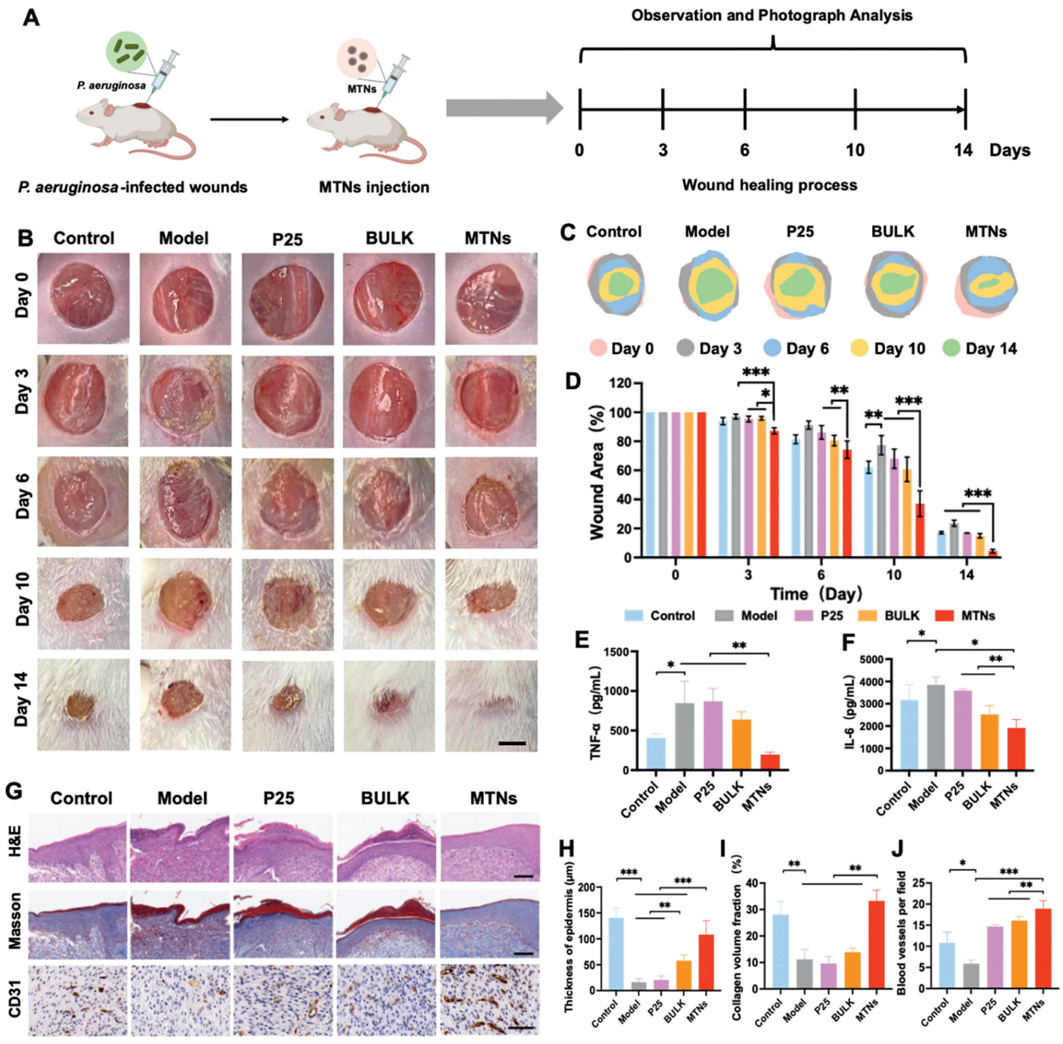

Fig. 3. *In vivo* performance of promoting *P. aeruginosa*-infected wound healing of MTNs. (A) Schematic construction and treatment of a *P. aeruginosa*-infected wound mouse model. (B) Representative images of wounds treated with MTNs, BULK, and P25 at different time points ($n = 6$; scale bar, 5 mm). (C) Corresponding schematic diagram of wound area changes at different time points. (D) Wound area (%) at different time points after treatment. (E, F) Levels of proinflammatory cytokines, including TNF-α and IL-6 on day 3, $n = 3$. (G) Representative images of H&E (scale bar, 100 μm), Masson's trichrome staining (scale bar, 100 μm), and immunohistochemistry staining of CD31 (scale bar, 50 μm) of the regenerated wound tissues on the 14th day, $n = 3$. (H–J) Corresponding quantification of epidermis thickness, collagen content, and regenerated blood vessels in wound tissues on the 14th day based on (G). Results are shown as mean ± SD. ($^{*}P < 0.05$, $^{**}P < 0.01$, and $^{***}P < 0.001$).

was 82.6%, 44.8%, and 15.3% for MTNs, BULK, and P25, respectively. The remarkedly greater loading content in MTNs might explained by their regular size and higher surface area. The biocompatibility of titanium nanoparticles was a critical prerequisite for their utilization in biomaterial applications [43–45]. The present study aimed to assess the cytotoxicity of titanium nanoparticles and OBZ-loaded nanoparticles using human immortalized epidermal cells (HaCaT). Herein, HaCaT cells were co-incubated with oxybenzone, titanium nanoparticles, and avobenzone-loaded titanium nanoparticles at various concentrations for 24 h. Our findings demonstrated that there was no obvious cytotoxicity at concentrations ranging from 1 μg/mL to 1000 μg/mL after a 24-h exposure of MTNs and OBZ-MTNs (Fig. S8 in Supporting information), while oxybenzone showed notable cytotoxicity at higher concentrations (Fig. S8G). MTNs, BULK, and P25 showed no evident cytotoxicity even at high concentrations, suggesting their excellent cytocompatibility and promising safety in practical application. Taken together, the results of our study indicated that both titanium nanoparticles and OBZ-loaded nanoparticles possessed good cytocompatibility and hold promise for further *in vivo* applications.

Since the antibacterial properties of MTNs, titanium dioxide has been explored as a potential inorganic sunscreen [46–48]. Due to MTNs have excellent mesoporous structure, which can be used as a carrier to support some UV filters. Beyond to be a carrier, MTNs could also be considered as a full-band physical sunscreen that protects against both UVA and UVB damage. The photoprotective activity of OBZ-loaded titanium nanoparticles were appraised in a murine model of photoaging. In detail, we exposed the backs of mice to a UVA lamp for 10 min to create a skin photodamage model (Fig. 4A). We applied different nanomaterials to the backs of the mice when they were exposed to UVA light, and monitored the back skin of mice 2 days later. As shown in Fig. 4B, the UVA-challenged skin showed severe peeling, scaling, and furrows. Such a photoaging mouse model used in the current study exhibited consistent clinical signs of wrinkling and laxity on the skin surface, similar to those observed in humans. By contrast, free OBZ, OBZ-loaded MTNs and OBZ-BULK significantly protected UVA-induced damage, while the OBZ-P25 exhibited serious erythema and damage. Notably, MTNs and BULK was able to load a greater measure of OBZ in comparison to P25 due to their mesoporous structure. Furthermore, the presence of the mesoporous structure might fa-

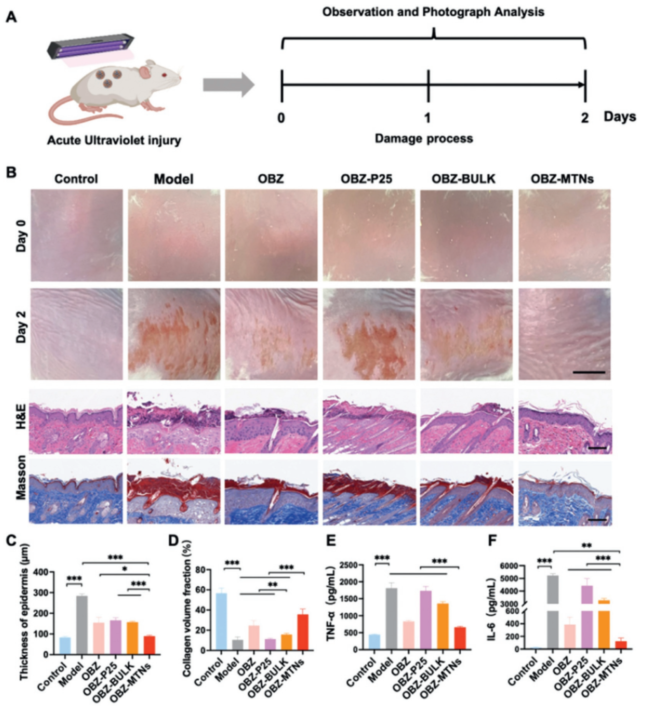

Fig. 4. Examination of UVA protection capability of OBZ-MTNs on mouse back skin. (A) Schematic construction of an acute ultraviolet injury mouse model. (B) Representative images of skin lesions treated with OBZ, OBZ-MTNs, OBZ-BULK and OBZ-P25 at different time points ($n = 6$; scale bar, 10 mm) and images of H&E (scale bar, 100 μm), Masson's trichrome staining (scale bar, 100 μm) of the skin tissues on the 2nd day, $n = 3$. (C, D) Corresponding quantification of epidermis thickness and collagen content in skin tissues on the 2nd day based on (A). (E, F) Levels of proinflammatory cytokines, including TNF-α and IL-6 on day 2, $n = 3$. Results are shown as mean ± SD ($^{*}P < 0.05$, $^{**}P < 0.01$, and $^{***}P < 0.001$).

cilitate superior UV absorption characteristics in OBZ-MTNs and OBZ-BULK. As expected, OBZ-MTNs outperformed OBZ-BULK and free OBZ in ameliorating furrow formation in UVA-irradiated skin. Epidermal thickness serves as a surrogate marker for skin edema severity, the phenotypic characterization of the skin was then captured *via* H&E staining images. The H&E pictures of skin demonstrated a marginal increase in epidermal thickness in the OBZ-MTN group, in contrast to the other compartments where a significant rise in thickness was observed (Fig. 4C). These findings were indicative of the exceptional UV absorption ability of OBZ-MTNs. Masson's trichrome staining also demonstrated that OBZ-MTNs group formed more collagen than other formulations (Fig. 4D). Additionally, we determined the levels of TNF-α and IL-6 in the skin since they play an important role in photodamage. As shown in Figs. 4E and F, OBZ-MTNs possessed the highest reduction of TNF-α and IL-6 levels, together demonstrating their great potential as a photoprotective agent against UVA-exposed skin. Finally, we evaluated the histopathological sections to demonstrate that there was no any systemic damage of main organs in all treatment groups (Fig. S9 in Supporting information).

In this study, we devised a sequential flash nanocomplexation strategy for scalable fabrication of mesoporous titanium nanoparticles with controlled particle size and uniformity for protecting UVA-exposed skin and improving infected wound healing. Having optimized the concentration of titanium precursor, PEG-functionalized silane and pH during the synthesis, the small size and mesoporous structure of MTNs were found to exhibit exceptional antibacterial properties when exposed to light, providing significant protection against UVA exposure-challenged skin damage in mice. The broad-spectrum antibacterial activities of MTNs were demonstrated against *E. coli*, *S. aureus*, and *P. aeruginosa* under light irradiation, and the nanoparticles were observed to accelerate *P. aeruginosa*-infected wound healing. With detailed *in vitro* and *in vivo* characterization, FNC-produced MTNs demonstrated the best performance than BULK and commercial P25 on photocatalytic and antibacterial activities. Our study expanded the capability of flash nanocomplexation as a continuous manufacture method to produce mesoporous titanium nanoparticles, thus allowing incorporating additional functionalities in a scalable fashion with ease. Such a simple method enabled the design and fabrication of mesoporous titanium nanoparticles with small size and large pore structures in a highly controllable manner, which was expected to be engineered to generate numerous delicate nanostructures with diverse compositions under facile and scalable conditions.

Declaration of competing interest

The authors declare that they have no known competing financial interests or personal relationships that could have appeared to influence the work reported in this paper.

Acknowledgment

This work was supported by the National Natural Science Foundation of China (No. 32271388).

Supplementary materials

Supplementary material associated with this article can be found, in the online version, at doi:10.1016/j.cclet.2023.108681.

References

[1] G. Liu, H.G. Yang, J. Pan, et al., Chem. Rev. 114 (2014) 9559–9612.
[2] A. Fujishima, K. Honda, Nature 238 (1972) 37–38.
[3] O. Khaselev, J.A. Turner, Science 280 (1998) 425–427.
[4] Z. Zou, J. Ye, K. Sayama, H. Arakawa, Nature 414 (2001) 625–627.
[5] S.U. Khan, M. Al-Shahry, W.B. Ingler Jr, Science 297 (2002) 2243–2245.
[6] C. Qin, J. Tang, R. Qiao, S. Lin, Chin. Chem. Lett. 33 (2022) 5218–5222.
[7] R. Asahi, T. Morikawa, T. Ohwaki, K. Aoki, Y. Taga, Science 293 (2001) 269–271.
[8] G. Dransfield, Radiat. Prot. Dosim. 91 (2000) 271–273.
[9] X.R. Wang, Y. Li, L.P. Tang, et al., Chin. Chem. Lett. 28 (2017) 394–399.
[10] H.M. Yadav, J.S. Kim, S.H. Pawar, Korean J. Chem. Eng. 33 (2016) 1989–1998.
[11] D. Li, H. Zhou, I. Honma, Nat. Mater. 3 (2004) 65–72.
[12] G. Zhang, H.B. Wu, T. Song, U. Paik, X.W. Lou, Angew. Chem. Int. Ed. 53 (2014) 12590–12593.
[13] H. Li, Z. Bian, J. Zhu, et al., J. Am. Chem. Soc. 129 (2007) 8406–8407.
[14] D. Chen, F. Huang, Y.B. Cheng, R.A. Caruso, Adv. Mater. 21 (2009) 2206–2210.
[15] H. Wu, C. Jia, M. Wang, et al., Chin. Chem. Lett. 33 (2022) 1983–1987.
[16] D.M. Antonelli, J.Y. Ying, Angew. Chem. Int. Ed. 34 (1995) 2014–2017.
[17] Y. Liu, R. Che, G. Chen, et al., Sci. Adv. 1 (2015) e1500166.
[18] H. Hu, C. Yang, M. Li, et al., Mater. Today 42 (2021) 99–116.
[19] W.S. Saad, R.K. Prud'homme, Nano Today 11 (2016) 212–227.
[20] S. Bobbala, S.D. Allen, E.A. Scott, Nanoscale 10 (2018) 5078–5088.
[21] H. Hu, C. Yang, F. Zhang, et al., Adv. Sci. 8 (2021) 2002020.
[22] H. Yan, D. Shao, Y.H. Lao, et al., Adv. Sci. 6 (2019) 1900605.
[23] Z. Fu, L. Li, Y. Wang, Q. Chen, X. Guo, Chem. Eng. J. 382 (2019) 122905.
[24] Z. Liu, A. Passalacqua, M.G. Olsen, R.O. Fox, J.C. Hill, AIChE J. 62 (2016) 2570–2578.
[25] Z. Zhu, P. Xu, G. Fan, et al., Chem. Eng. J. 356 (2019) 877–885.
[26] Z. Fu, L. Li, M. Wang, X. Guo, Colloid Polym. Sci. 296 (2018) 935–940.
[27] R. Sharma, A. Sarkar, R. Jha, A. Kumar Sharma, D. Sharma, Int. J. Appl. Ceram. Technol. 17 (2020) 1400–1409.
[28] R. Zhang, B. Tu, D. Zhao, Chem. Eur. J. 16 (2010) 9977–9981.
[29] G. Liu, Y. Zhao, C. Sun, et al., Angew. Chem. Int. Ed. 47 (2008) 4516–4520.
[30] A.L. Linsebigler, G. Lu, J.T. Yates Jr, Chem. Rev. 95 (1995) 735–758.
[31] Q. Guo, C. Zhou, Z. Ma, X. Yang, Adv. Mater. 31 (2019) e1901997.
[32] J. Schneider, M. Matsuoka, M. Takeuchi, et al., Chem. Rev. 114 (2014) 9919–9986.
[33] T. Luttrell, S. Halpegamage, J. Tao, et al., Sci. Rep. 4 (2014) 4043.
[34] J. Ding, J. Zhang, J. Li, et al., Prog. Polym. Sci. 90 (2019) 1–34.
[35] X. Wan, Y. Zhao, Z. Li, L. Li, Exploration 2 (2022) 20210029.
[36] Y. Zhang, Y. Xu, H. Kong, et al., Exploration 3 (2023) 20210170.
[37] T. Liu, G. Liu, J. Zhang, et al., Chin. Chem. Lett. 33 (2022) 1880–1884.
[38] G. Liu, Y. Zhou, Z. Xu, et al., Chin. Chem. Lett. 34 (2023) 107705.

[39] J.B. Acosta, D.G. del Barco, D.C. Vera, et al., Int. Wound J. 5 (2008) 530–539.
[40] R. Zhao, H. Liang, E. Clarke, C. Jackson, M. Xue, Int. J. Mol. Sci. 17 (2016) 2085.
[41] X. Wang, M. Zhang, T. Zhu, et al., Adv. Sci. 10 (2023) e2206154.
[42] R. Li, K. Liu, X. Huang, et al., Adv. Sci. 9 (2022) e2105152.
[43] R. Zhang, A.A. Elzatahry, S.S. Al-Deyab, D. Zhao, Nano Today 7 (2012) 344–366.
[44] A.T. Sidambe, Materials 7 (2014) 8168–8188.
[45] T. Hanawa, Sci. Technol. Adv. Mater. 23 (2022) 457–472.
[46] K.M. Tyner, A.M. Wokovich, D.E. Godar, W.H. Doub, N. Sadrieh, Int. J. Cosmet. Sci. 33 (2011) 234–244.
[47] M. Vujovic, E. Kostic, J. Cosmet. Sci. 70 (2019) 223–234.
[48] S.L. Schneider, H.W. Lim, Photodermatol. Photoimmunol. Photomed. 35 (2019) 442–446.